Journal of Structural Geology 115 (2018) 152–166

Contents lists available at ScienceDirect

Journal of Structural Geology

journal homepage: www.elsevier.com/locate/jsg

Mechanics and microstructure of deformed natural anisotropic ice

Lisa Craw[a,*], Chao Qi[b], David J. Prior[a], David L. Goldsby[b], Daeyeong Kim[c]

[a] Department of Geology, University of Otago, Dunedin, New Zealand
[b] Department of Earth and Environmental Science, University of Pennsylvania, Philadelphia, PA, USA
[c] Division of Polar Earth-System Sciences, Korea Polar Research Institute, Incheon, South Korea

ARTICLE INFO

Keywords:
Ice deformation
Glaciology
Ice microstructure
Grain boundary sliding
Crystallographic preferred orientations

ABSTRACT

We deformed coarse-grained (~10 mm) natural ice in axial compression at −30 °C, to an axial strain of 0.2, at three different angles to the existing strong crystallographic preferred orientation (CPO). We used three strain rates for each sample orientation. Cryo-electron backscatter diffraction (EBSD) maps show that after deformation there is a mixture of large (~1–2 mm) relict grains, and finer (100–200 μm) recrystallised grains. The fine grains form a connected network in all samples. The large grains define a very strong CPO with equivalent but weaker CPOs in the recrystallised grains. The final CPO changed completely from its original orientation. Lattice distortion and subgrains equivalent in size to recrystallised grains suggest a subgrain rotation recrystallisation process has generated the recrystallised fraction. We suggest that strain rates were higher in the connected network of recrystallised grains because of a significant component of grain boundary sliding (GBS) that enables large grains to rotate by a combination of glide on the basal plane and rigid rotation, to define a very strong CPO. GBS weakens the CPO in the finer grained regions. The patterns of mechanical behaviour and the resultant microstructures do not bear an obvious relationship to original CPO.

1. Introduction

Ice 1h occurs naturally under Earth conditions, making up all glaciers, ice shelves and ice streams on the planet (Pauling, 1935). In a natural setting ice will flow under the influence of gravity, tidal forces, and other differential stresses, at rates controlled by stress magnitudes and temperature. A single ice crystal behaves anisotropically, as it is sixty times easier for strain to be accommodated through sliding on the basal, (0001) plane than on any other plane (Jones and Glen, 1969a; Duval et al., 1983). In addition, in polycrystalline ice, grains which are poorly oriented for basal slip accumulate higher internal distortion (Duval et al., 1983), and so are preferentially consumed and replaced by those which are better oriented for easy slip (Vaughan et al., 2017). As a result, when a differential stress is applied to an ice mass, a broader-scale anisotropy develops in the form of a crystallographic preferred orientation (CPO: also known as crystal orientation fabric or texture). Under low-temperature and high strain-rate conditions, crystallographic *c*-axes of ice grains within the mass favour a cluster parallel to the compression direction (as a result of lattice rotation through sliding on the basal plane), and under high-temperature and low strain-rate conditions they favour a hollow cone (small circle distribution) at 30–60° around compression (as a result of dynamic recrystallisation of preferentially oriented grains) (Alley, 1992; Qi et al., 2017).

Most laboratory studies examining the formation of CPOs in ice are performed on laboratory-made ice with no pre-existing anisotropy (see Kamb, 1972; Durham et al., 1983; Gao and Jacka, 1987; Budd et al., 2013, and many others). This guarantees a predictable isotropic starting material. However, these experiments can only represent a limited range of real glaciological scenarios, where ice with no strain history is subjected to a stress. An example of this is an ice dome, where snow is deposited in a random way, and then is slowly compacted into firn and then ice under compression (Dahl-Jensen et al., 1997; Wang et al., 2002). Experiments on isotropic ice do not provide robust insights into the behaviour of ice which has already been flowing, and therefore has a pre-existing CPO which may or may not be oriented optimally for the stresses it is experiencing. For example, polar ice which is flowing toward the sea in a glacier or ice stream in a kinematic regime of longitudinal extension can be subjected instead to longitudinal compression as a result of ice shelf buttressing at the coast retarding forward flow (Warner and Budd, 1998; Rignot et al., 2004; Treverrow et al., 2010). In this case, the ice mass must transition from one CPO to another in line with the stresses present, and the rate of this response has major implications for understanding the effects of ice shelf collapse due to global climate change (Hughes, 2009; Hudleston, 2015).

In addition to CPO, natural ice contains a wide range of mechanical heterogeneities in the form of bubbles (Shoji and Langway, 1982;

* Corresponding author.
E-mail addresses: crali915@student.otago.ac.nz (L. Craw), david.prior@otago.ac.nz (D.J. Prior).

https://doi.org/10.1016/j.jsg.2018.07.014
Received 1 February 2018; Received in revised form 13 July 2018; Accepted 19 July 2018
Available online 30 July 2018
0191-8141/

Table 1
Experimental parameters from previous studies using natural ice, alongside those from the current study.

	sample origin	starting CPO	T (°C)	σ_{ax} (MPa) [a]	ε_{ax} [b]
Gao and Jacka, 1987	Law Dome, East Antarctica	vertical cluster	−3.3	0.42	0.21
Dahl-Jensen et al., 1997	GRIP core, central Greenland	vertical cluster	−16	0.64	0.3
Castelnau et al., 1998	GRIP core, central Greenland	vertical cluster	−10, −15	0.28–0.63	0.006–0.01
Dierckx et al., 2014	Nansen Ice Shelf, Antarctica	vertical cluster	−6.0	0.21–1.7	0.05
Treverrow et al., 2012	Law Dome, East Antarctica	vertical cluster, cone	−2.0	0.42–1.7	0.23
current study	Tarn Flat, Antarctica	girdle	−30	Constant displacement rate	0.2

[a] σ_{ax} is the axial stress applied to the sample.
[b] ε_{ax} is the maximum axial strain reached.

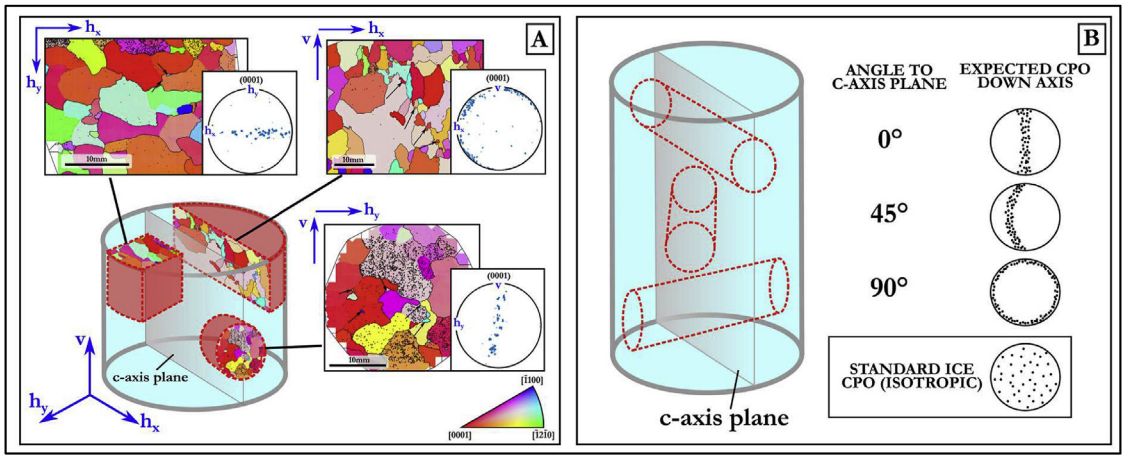

Fig. 1. Orientation of the vertical girdle CPO in the original ice cores. A) orientation maps and accompanying stereonets of *c*-axis orientations from 10,000 randomly selected pixels. The original orientations of the planes are shown schematically in the bottom left, along with the reference frame used. Maps are coloured according to the crystallographic direction which is parallel to the vertical (v), according to the legend in the bottom right. B) the orientations of sub-cores relative to their parent core and the *c*-axis orientation plane, with expected CPOs down the sub-core axis.

Barnes and Wolff, 2004), changing rheology as a result of foliation (Hambrey, 1975; Hudleston and Hooke, 1980) and solid impurities (Baker and Gerberich, 1979; Barnes et al., 2002), alongside aqueous chemical impurities which can affect its mechanical and microstructural properties (Jones and Glen, 1969b; Baker et al., 2003; Hammonds and Baker, 2016). The purpose of this study is to understand the way in which real Antarctic ice responds to a changing stress system, and how the presence of impurities, imperfections and a pre-existing CPO affect this response.

1.1. Previous work

There have been some previous studies investigating the deformation of ice with a pre-existing CPO, under the experimental conditions summarised in Table 1. Gao and Jacka (1987) deformed ice from Law Dome, Antarctica, some with a cone CPO and some with a cluster CPO. They found that ice with a CPO which was favourably oriented for the differential stresses applied to it (i.e., most grains had a high Schmid factor) experienced a higher minimum strain rate, proceeding almost directly from primary to tertiary stages of creep. Later work by Treverrow et al. (2012) has replicated this. Dahl-Jensen et al. (1997) performed compression tests on ice from the Greenland Ice core Project (GRIP) with varying strengths of CPO, deforming samples for up to three years at vertical stresses of 0.64 MPa, and concluded that once the tertiary strain stage had been reached and a new CPO developed according to stress and temperature conditions, the original flow conditions of the ice had no remaining mechanical effects on behaviour. Similar tests on ice from the same cores by Castelnau et al. (1998) found that ice with a stronger CPO (taken from a greater depth) displayed rheological behaviours with stronger anisotropy. While all of those studies focussed on ice with a compressional CPO (*c*-axis cluster or cone) which is close to optimally oriented for the applied stresses, Dierckx et al. (2014) is an exception, applying unconfined uniaxial compression to marine folded ice from the Nansen Ice Shelf, Antarctica, cut at different angles to a fold axis. The study found that samples cut at "hard slip" orientations (at either 0° or 90° to the fold axis) were harder to deform than weakly textured ice, with stress exponents ranging from n = 3.2–4.1, and samples cut at "easy slip" orientations (45° to the fold axis) were easier to deform, with a stress exponent of n = 4.1.

It is important to note that all of these precursor studies have been performed at temperatures of −16° or higher, and vertical stresses of less than 2 MPa. This current study aims to build on their results by both extending the range of experimental conditions to lower temperatures and higher stresses, and using recent cryo-EBSD technology to provide a more thorough microstructural analysis than has previously been possible.

2. Experimental methods

2.1. Sample preparation

The original ice cores were collected by the Korea Polar Research Institute during the 2016–2017 field season, from the near surface (1–2 m depth) at Tarn Flat, Antarctica. This is a "blue glacier" area where ice has been brought to the surface from greater depths. The ice cores contain through-going planar features visible at the surface of the core as pale white lines of porosity, possibly related to healed fractures. A hospital CT scan of this core confirms the planar nature and consistent high porosity of these features. An initial series of EBSD measurements were made of the core material, revealing it to have a vertical girdle *c*-axis distribution (Fig. 1A). Sub-samples for deformation were extracted from the cores at known angles of 0°, 45° and 90° to the

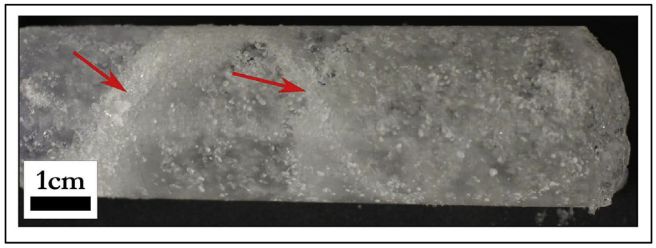

Fig. 2. Photograph of a sub-core as extracted from the main ice core (collected from approximately one metre's depth), showing planes of high porosity (red arrows) emerging on the surface. (For interpretation of the references to colour in this figure legend, the reader is referred to the Web version of this article.)

girdle orientation (*c*-axis plane, Fig. 1B). The orientation maps also revealed the presence of bubbles between 0.25 and 2 mm, localised along the planar porosity features (Fig. 2).

Sub-cores were drilled out of the larger cores using a one-inch coring piece (ROTABROACH annular cutter) attached to a milling machine in a cold room at −20 °C. This produced samples of 25.4 mm in diameter, and approximately 80 mm in length. There was some breakage around irregular areas of the ice. These samples were shortened and the ends flattened with a razor blade in a −30 °C freezer, with the final target length being 56 mm (2.2 inches). They were then encased in indium jackets, which were soldered onto steel spacers at one end and a force gauge at the other. A zirconium spacer was inserted between the sample and the force gauge to insulate the ice from heat during the soldering process. Due to the high porosity of the samples, the indium jackets were prone to puncture once they reached 30 MPa pressure. To prevent this, some samples were double-jacketed.

To act as a control, synthetic ice samples were prepared using the technique described by Durham et al. (1983) and Stern et al. (1989). Ice made from deionised water was iteratively crushed in a blender and sieved to produce seed grains with sizes between 180 and 250 μm. These grains were packed into cylindrical moulds with an interior diameter of 25.4 mm (1 inch), and flooded under vacuum by deionised water with a temperature of precisely 0 °C. The moulds were then left overnight in a −30 °C freezer in polystyrene insulation, with their bases resting on a copper sheet and their top plugs removed. This forced the ice to freeze from the bottom up, and the result was samples with < 1% porosity, no significant impurities, and an average grain size of 230 μm (Qi et al., 2017).

2.2. Experimental procedure

These experiments were performed in the Ice Physics Laboratory at the Department of Earth and Environmental Science, University of Pennsylvania. The apparatus is a custom-built, fixed-rate axial deformation rig with gas medium pressure regulation, cooled by a circulating alcohol bath (Durham et al., 1983). All experiments were performed at a constant strain rate to a true axial strain of ≥0.2., at a temperature of −30 ± 0.5 °C and 20 ± 0.5 MPa of confining pressure.

Before deformation, samples were inserted into the apparatus, pressurised and left for 1–2 h, allowing temperatures to equilibrate and larger pores to close. The temperatures of the circulating alcohol bath, and both upper and lower pistons were logged throughout the experiments, along with load on an internal force gauge and piston displacement. Once a strain of > 0.2 was reached, the load was removed, and within several minutes the chamber was brought down to atmospheric pressure, and the samples were removed from the apparatus and transferred to a −30 °C freezer for storage.

Parameters for all experiments are presented in Table 2. For all of the three orientations, one sample was deformed at a high ($\approx 2 \times 10^{-5}$ s^{-1}), intermediate ($\approx 5 \times 10^{-6}$ s^{-1}) and low ($\approx 2 \times 10^{-6}$ s^{-1}) strain rate. One sample, which was drilled at 45° to the *c*-axis plane, broke along a pre-existing fracture and could not be deformed. For this reason, there is no "45°" sample deformed at an intermediate strain rate. Each sample was given a PIL number according to convention at the Penn Ice Lab.

2.3. Mechanical data processing

The raw data recorded during an experiment were: time, piston displacement, temperature of upper and lower pistons, and load on the force gauge. Temperatures remained within 0.5 °C of the target temperature of −30 °C at all times during deformation. The piston displacement was used to derive the sample length at each time value, and along with the measured initial length could be used to calculate true axial strain using equation (1) (Means, 1976), where L_o is the initial length of the sample, and L_f is its length at any given time:

$$\varepsilon = \ln\left(\frac{L_0}{L_f}\right) \quad (1)$$

Stress was derived from load and cross-sectional area, and simple corrections were applied for the increase in cross-sectional area (assuming constant volume) as deformation proceeded.

2.4. Microstructural analysis

After deformation at the University of Pennsylvania Ice Physics Laboratory, samples were transported back to Otago in a nitrogen dry shipper, and stored in dewars of liquid nitrogen at or close to −196 °C. The routine for preparing for and performing cryo-EBSD analysis at the Otago Centre for Electron Microscopy is described in detail by Prior et al. (2015) and is described here only briefly.

Firstly, the cylindrical samples were cut into two axially, with one piece returned to storage for future use. This was done with the indium jacket still attached, to avoid fragmentation. Next, the temperature of the sample was gradually raised to −20 °C, and the flat face was placed against a copper ingot at +5–8 °C, allowing a thin film of water to melt and refreeze as pressure was applied, and fixing the sample to the ingot. The indium jacket was then removed, and the opposing, rounded face ground down manually against 100-grit sandpaper to expose a flat interior surface for examination. This surface was polished by a sequence of finer sandpapers, finishing with a 1200-grit grinding plate. After this process was completed at temperatures between −40 and −20 °C, the sample was gradually cooled to below −90 °C.

The Scanning Electron Microscope (SEM) used is a Zeiss Sigma variable pressure field-emission-gun SEM fitted with a Nordlys EBSD camera from Oxford Instruments and equipped with a custom cryo-stage cooled via a copper braid connection to a continually filled external liquid nitrogen dewar. In preparation for ice measurements, the cryo-stage was cooled to below −100 °C. the sample could then be transferred to the stage via an enclosed chamber filled with gaseous nitrogen, to avoid the build-up of frost on the ice surface. During the transfer process, the temperature of the ice did not exceed −80 °C.

Finally, a "sublimation cycle" was run, by releasing the vacuum in the SEM chamber and allowing the stage temperature to rise to between −75 and −80 °C, before restoring vacuum. The second stage of this cycle, as the lowering of temperature lags behind the pressure change, allows any frost to sublime and fully exposes an undamaged surface (Prior et al., 2015).

Full cross-sectional orientation maps were collected for all samples at 30 μm step size (in the case of PIL141 this was done in two parts). In addition, high spatial resolution (step sizes of 2–10 μm) and high angular resolution maps with the EBSD camera retracted (Prior et al., 1999) were collected from smaller areas where data quality permitted.

All EBSD data were collected using Oxford Instruments AZtec software, and subsequently exported into HKL Channel 5. Original data

Table 2
Experimental parameters and mechanical data from all experiments.

sample	orientation[a]	L_0	σ_y[b]	$\dot{\varepsilon}_y$[c]	σ_f	$\dot{\varepsilon}_f$	peak grain size	mean grain size	ε[d]
		mm	MPa	s^{-1}	MPa	s^{-1}	μm	μm	
PIL140	0	50.8	4.52	2.2×10^{-6}	3.88	2.3×10^{-6}	140	225	0.21
PIL138	45	45.72	4.53	2.3×10^{-6}	3.78	2.4×10^{-6}	260	326	0.22
PIL129	90	49.53	2.8	2.6×10^{-6}	–	–	140	278	0.22
PIL133	isotropic	59.436	6.52	2.3×10^{-6}	4.84	2.6×10^{-6}	140	223	0.20
PIL134	0	60.96	7.98	6.7×10^{-6}	4.58	7.3×10^{-6}	180	280	0.20
PIL130	90	53.086	4.22	6.3×10^{-6}	–	–	160	316	0.20
PIL141	isotropic	54.356	7.64	6×10^{-6}	5.06	7.2×10^{-6}	140	199	0.23
PIL136	0	73.152	3.75	1.9×10^{-5}	–	–	120	326	0.23
PIL139	45	41.148	5.96	2.3×10^{-5}	4.03	2.6×10^{-5}	140	250	0.23
PIL131	90	49.022	6.8	2.4×10^{-5}	–	–	180	306	0.22
PIL132	isotropic	54.864	11	2.1×10^{-5}	6.92	2.8×10^{-5}	140	216	0.20

[a] Denotes the orientation of the compression direction to the *c*-axis plane (see Fig. 1).
[b] σ_y and σ_f are the axial normal yield and flow stresses.
[c] $\dot{\varepsilon}_y$ and $\dot{\varepsilon}_f$ are the axial normal strain rates at the peak and flow stresses.
[d] ε is the maximum true strain reached.

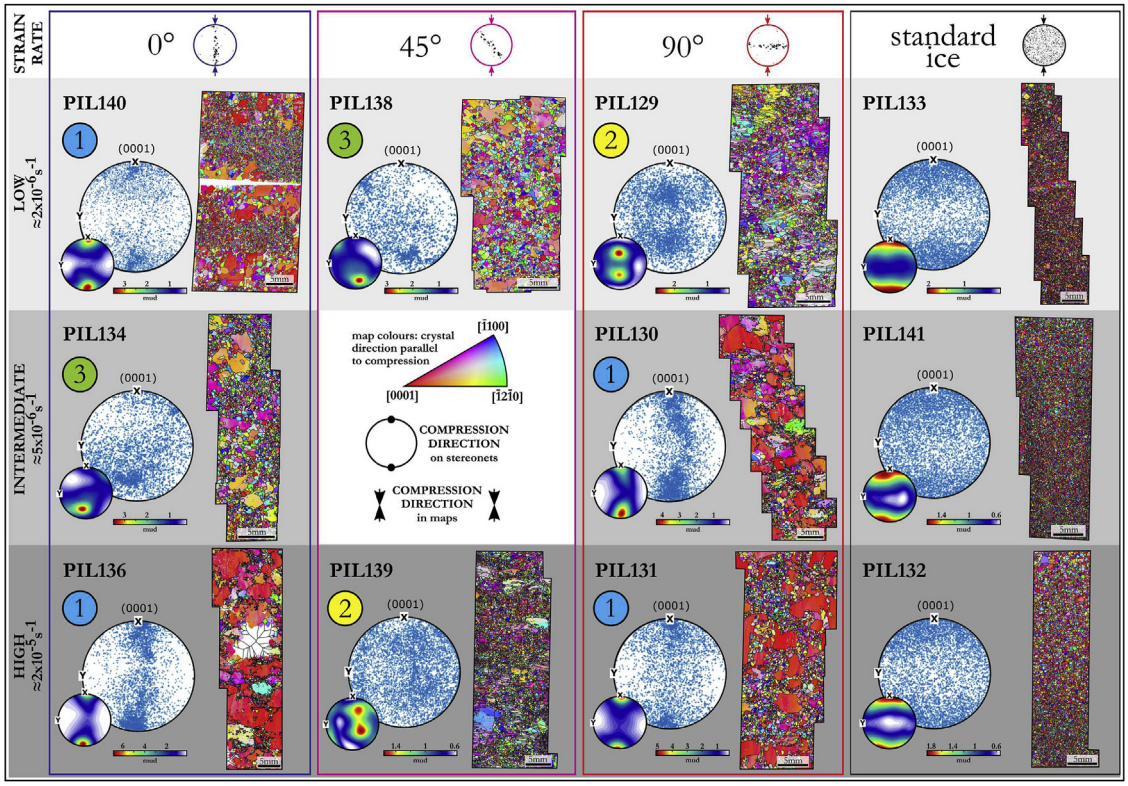

Fig. 3. Cross-sectional orientation maps of all samples alongside lower hemisphere, equal area stereonets showing the *c*-axis orientations for a random selection of 10,000 pixels. Smaller pole figures show orientation data of all indexed pixels contoured by multiples of uniform density (mud). Map colours indicate the crystallographic direction which is parallel to compression (vertical here) according to the inverse pole figure legend in the centre. Each column shows all the experiments with a particular initial CPO, indicated by the stereonet at the top of the column. In each column, data are organised by increasing strain rate downwards with the strain rates shown on the left-hand side. Circled numbers denote microstructural grouping, as discussed in the text. Column border colours and numbered circle fill colours are used to indicate initial CPO and microstructural group in Fig. 11. (For interpretation of the references to colour in this figure legend, the reader is referred to the Web version of this article.)

quality is variable, due to factors such as sample surface quality and variations in sublimation. To improve data quality, the MATLAB program EBSDInterp 1.0, developed by Pearce (2015) was used. This program uses band contrast as a template for noise reduction. The remainder of the processing was performed in MTEX, a texture analysis software package which runs on the MATLAB platform (Bachmann et al., 2011; Mainprice et al., 2015). MTEX algorithms were used to produce robust microstructural analysis by defining grain boundaries, producing pole figures of lattice orientations, and segmenting grains by size, location and orientation. In some cases, the program HKL Channel 5 was used to produce misorientation profiles. At every stage, grain boundaries are defined as boundaries with a misorientation of ≥15°.

3. Results

3.1. Microstructural data

Cross-sectional orientation maps and pole figures of *c*-axis

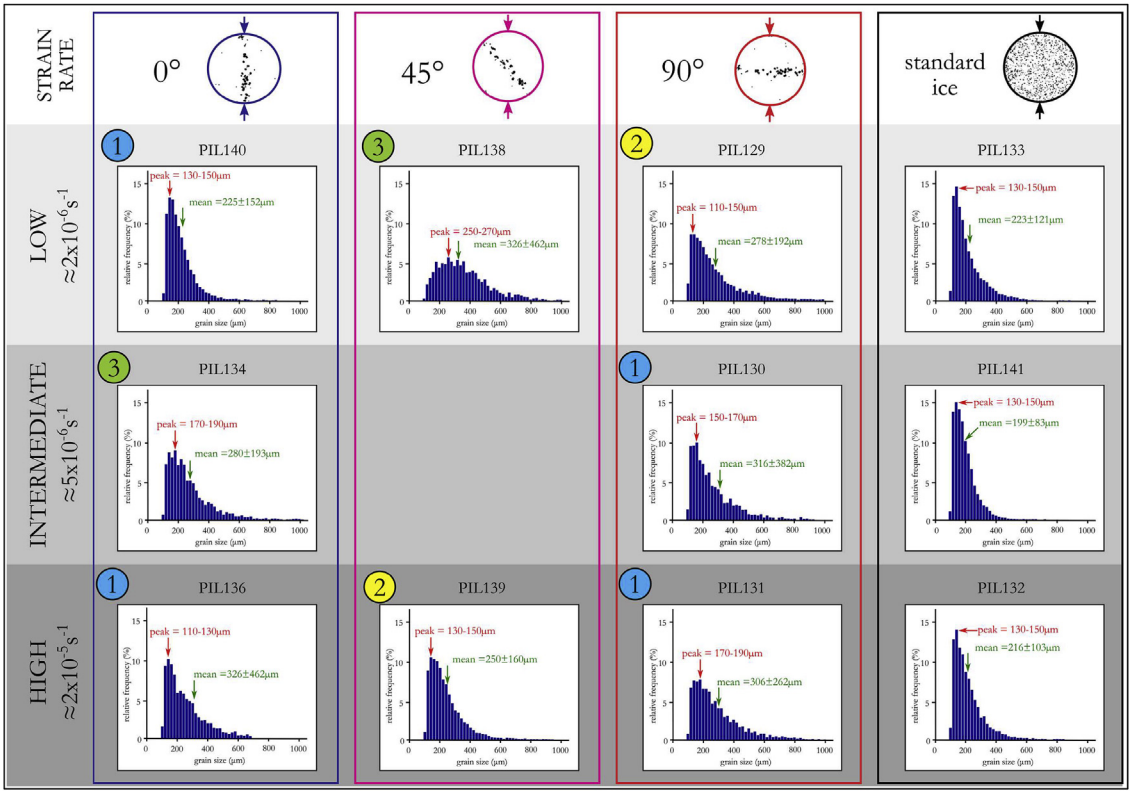

Fig. 4. Histograms of grain sizes (area equivalent diameter) of all samples, as derived from the orientation maps in Fig. 3. Mean grain sizes and those which occur with peak frequency are indicated. Each column shows all the experiments with a particular initial CPO, indicated by the stereonet at the top of the column. In each column, data are organised by increasing strain rate downwards with the strain rates shown on the left-hand side. Circled numbers denote microstructural grouping, as discussed in the text.

orientation for all samples are shown in Fig. 3, and grain size histograms in Fig. 4. Grain size data are also displayed in Table 2. Natural samples exhibit a high degree of heterogeneity in contrast to those made from laboratory ice, which are much more consistent.

3.1.1. Synthetic "standard" ice

The undeformed standard ice was not analysed for this study, however Qi et al. (2017) provide EBSD data from equivalent ice prepared using the same equipment and methods. The standard ice starting material is isotropic, with largely straight boundaries, polygonal grains, and grain sizes approximating a normal distribution around a mean of 230 μm. There is virtually no distortion within grains.

The deformed standard ice samples, PIL141, PIL132 and PIL133 (listed in order of decreasing strain rate) exhibit mean grain sizes of 216 μm, 199 μm and 223 μm respectively, covering a range from 100–800 μm, but with ≈85% of grains falling within the 150–250 μm range. The distribution of grain sizes after deformation has evolved away from its originally normal distribution to an asymmetric shape, with peak grain sizes significantly smaller than the mean in all cases, and a distinctive "tail" extending to grain sizes larger than those existing in the starting material.

High resolution images show that grain boundaries are slightly lobate, however there is no obvious shape-preferred orientation. Some grains contain low angle boundaries and are characterised by a high kernel average misorientation (KAM) concentrated along linear features. Much smaller (20–80 μm) grains are present along grain and subgrain boundaries. Pole figure plots of *c*-axis orientations show that all three standard ice samples exhibit a cluster of *c*-axes oriented parallel to the axis of compression. The *c*-axis clusters are relatively weak, with maximum multiples of uniform density of 1.6–2.1.

3.1.2. Natural ice

Prior to experimental deformation, the original core ice comprises irregularly shaped grains up to 15 mm in diameter, with slightly lobate boundaries. Unfortunately, the small size of the studied sections relative to the grain size did not allow meaningful grain size statistics to be produced for the natural ice prior to deformation, although the maps in Fig. 1 indicate that mean grain size is likely to be several mm.

After deformation, the microstructural characteristics of the samples are more complex and heterogeneous. Beginning with their common features, all post-deformation samples contain both large (800–1000 μm) and very fine (< 300 μm) grains, where the CPO is strongly defined by the larger grains, and much more diffuse in the finer fraction (Fig. 5). Finer grains have little internal distortion and boundaries which are straight or slightly curved, while larger grains have very lobate boundaries and internal distortion to varying degrees, including subgrain boundaries near the grain margins which define subgrains similar in size to the finer grains. Grain sizes (area equivalent diameter) show an asymmetric distribution, with the mean size larger than the most frequently occurring size range in all cases, by an average of 120 μm (Fig. 4). All grains in the deformed samples are smaller than the vast majority of grains in the original core material. Low angle (3–25°) grain boundaries occur with greater frequency than that predicted from the CPO (random pair misorientations: Wheeler et al., 2001) in all samples.

On the basis of their microstructural characteristics, these deformed samples can be broadly divided into three groups, which are not obviously correlated with specific strain rates or starting CPO orientations (although it is not possible to be certain with such a small number of samples). The microstructural characteristics of each group in turn will be discussed.

Group 1 consists of samples PIL130 (intermediate strain rate, 90° starting CPO); PIL131 (high strain rate, 90° starting CPO); PIL136 (high

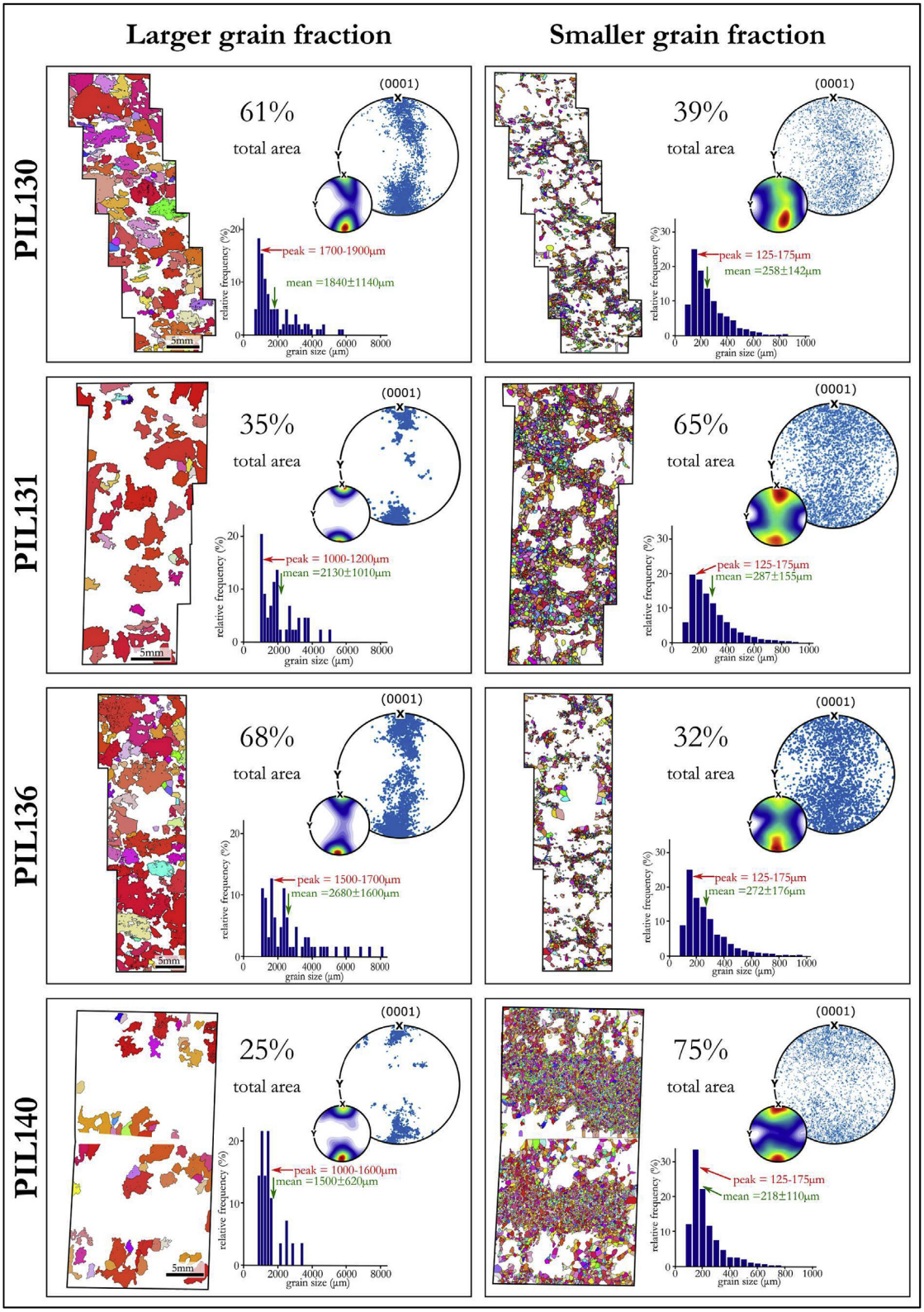

Fig. 5. EBSD orientation maps, grain size distribution histograms and *c*-axis orientation pole figures for the samples in microstructural group 1 (see text), with grains segregated by size (area equivalent diameter). Pole figures show *c*-axis orientations of a random selection of 10,000 pixels, alongside contoured figures of all indexed pixels. Map colours indicate the crystallographic direction which is parallel to shortening (vertical), according to the inverse pole figure legend in Fig. 3. (For interpretation of the references to colour in this figure legend, the reader is referred to the Web version of this article.)

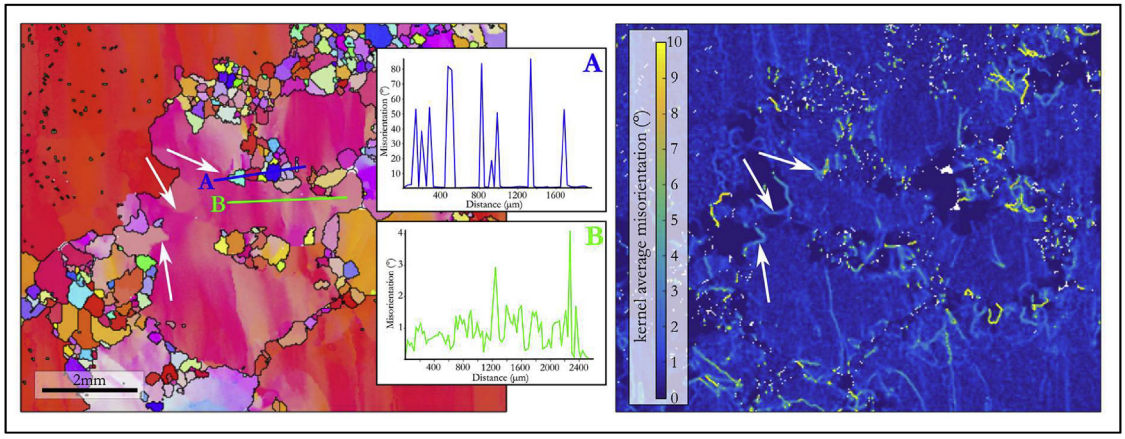

Fig. 6. Smaller grains within a larger grain in sample PIL136. Left, a high-resolution orientation map of the area, with colours indicating the crystallographic direction which is parallel to compression (vertical), according to the inverse pole figure legend shown in Fig. 3. Inset, plots of misorientation along profile A and B as indicated on the map. Right, map of kernel average misorientation angle excluding grain boundaries. White arrows indicate examples of sub-grain boundaries. (For interpretation of the references to colour in this figure legend, the reader is referred to the Web version of this article.)

strain rate, 0° starting CPO); and PIL140 (low strain rate, 0° starting CPO). All of these samples have a strong *c*-axis cluster parallel to the shortening direction. They are also distinguished by clear structures of large grains (> 800 μm), surrounded by an interconnected network of much smaller (typically < 300 μm) grains. In Fig. 5, orientation maps of these samples filtered by grain size show this structure clearly.

There are also several cases in this group of finer grains appearing within larger grains. Fig. 6 shows an example of this from PIL136, with misorientation profiles across a row of smaller grains (Fig. 6A) and an intact but deformed section of larger grain adjacent (Fig. 6B). Boundary misorientations between the finer grains are commonly as high as 60–80°, while the larger grain contains a series of 0–4° misorientations characteristic of lattice bending. Subgrain boundaries occur at the edges of larger grains, indicated by white arrows, defining subgrains similar in size to the smaller grains adjacent to them. A map of kernel average misorientation over the same area (Fig. 6, right) shows a high level of distortion within larger grains, and virtually none within the finer grains.

PIL140 is slightly different, displaying what appear to be layers of exclusively smaller grains, alternating with layers more similar to the other samples in this group; that is, larger grains surrounded by an interconnected network of smaller grains. These layers are sub-perpendicular to the compression direction and are on a scale of 5–10 mm.

Group 2 consists of samples PIL129 (low strain rate, 0° starting CPO), and PIL139 (high strain rate, 45° starting orientation). These samples are distinctive for their double-cluster CPOs and the widespread occurrence of kink structures with boundary traces oriented sub-perpendicular to the compression direction where they intercept the plane of view. There are some larger (> 800 μm) grains, but most are segmented into 100–500 μm thick kink bands. The remainder of the grains make up a much finer (100–800 μm) matrix. As shown in Fig. 7, the two *c*-axis clusters lie in the same vertical plane, and correspond to sections of grains within the mass on the 3–6 mm scale, the *c*-axes of which are oriented 40°–60° from the compression direction. These sections are distributed unevenly throughout the samples.

It is difficult to separate grains in these samples into distinct "smaller" and "larger" fractions due to kinking breaking larger grains into irregular shapes and sizes. However, PIL129 and PIL139 have average grain sizes of 250 ± 160 μm and 278 ± 192 μm respectively.

Finally, group 3 consists of samples PIL134 (intermediate strain rate, 0° starting CPO) and PIL138 (low strain rate, 45° starting CPO). These samples both have cluster CPOs which are inclined 30–40° from the compression direction, and their grain size distributions are more rounded and lack a strongly defined peak. Fig. 8 shows several orientation maps of both samples segregated by grain size. Some very large (> 800 μm grains) are present, with strong internal distortion, and there are also many very small (> 300 μm) grains with little to no internal distortion. However, these samples also contain a proportion of around ⅓ medium sized 300–800 μm grains, which are irregularly shaped and contain evenly distributed distortion gradients and sub-grain boundaries. As in other samples, the larger grains define the CPO most strongly, and the finer grains have a near-isotropic CPO. The medium sized grains do define the same CPO as the larger grains, but much more weakly. Very small grains often occur within these mid-sized grains, at sub-grain boundaries and between grains.

3.2. Mechanical data

After extraction from the deformation apparatus, the samples were photographed while still in their indium jackets. Examples of these are shown in Fig. 9. Samples of standard ice appear smooth, although the thickness of the double indium jackets may be obscuring details on a millimetre scale. Natural samples are more irregular in appearance, with a surface texture characterised by "lumpiness" on the 2–5 mm scale. We infer that sharp dimples on the surface identify points where the indium has moved inward to close a large pore. These samples have bulged outward horizontally, but the bulging is in many cases irregularly distributed on the centimetre scale. In some cases the upper and lower pistons are slightly misaligned after deformation, with a horizontal offset of 0.5–1 mm.

The indium jackets will support some of the load applied to the sample. A full correction that assumes the jacket is a thin walled cylinder, using unpublished indium rheology data (from W.B. Durham), would reduce stresses by up to 2 MPa (changing the final value of the stress exponent for standard ice to n = 3.1 and leaving that of the 90° samples virtually unchanged). However, because of jacket bending the jacket does not carry the full load implicit in the thin walled cylinder model, and so the true correction is likely to be much less. For simplicity we have chosen to present the data with no indium jacket corrections.

Plots of stress versus true strain for all experiments are shown in Fig. 10. The "yield stress" for each experiment is taken as the stress at which the first high-gradient segment of the graph transitions to a much lower gradient within a small increment of strain. This is broadly equivalent to the "peak stress" recorded in other studies (e.g. Qi et al., 2017), but as there are cases here where the flow stress is higher, the term "peak stress" will not be used for the sake of clarity. The "flow stress" is taken as the near-constant stress approached at high strains

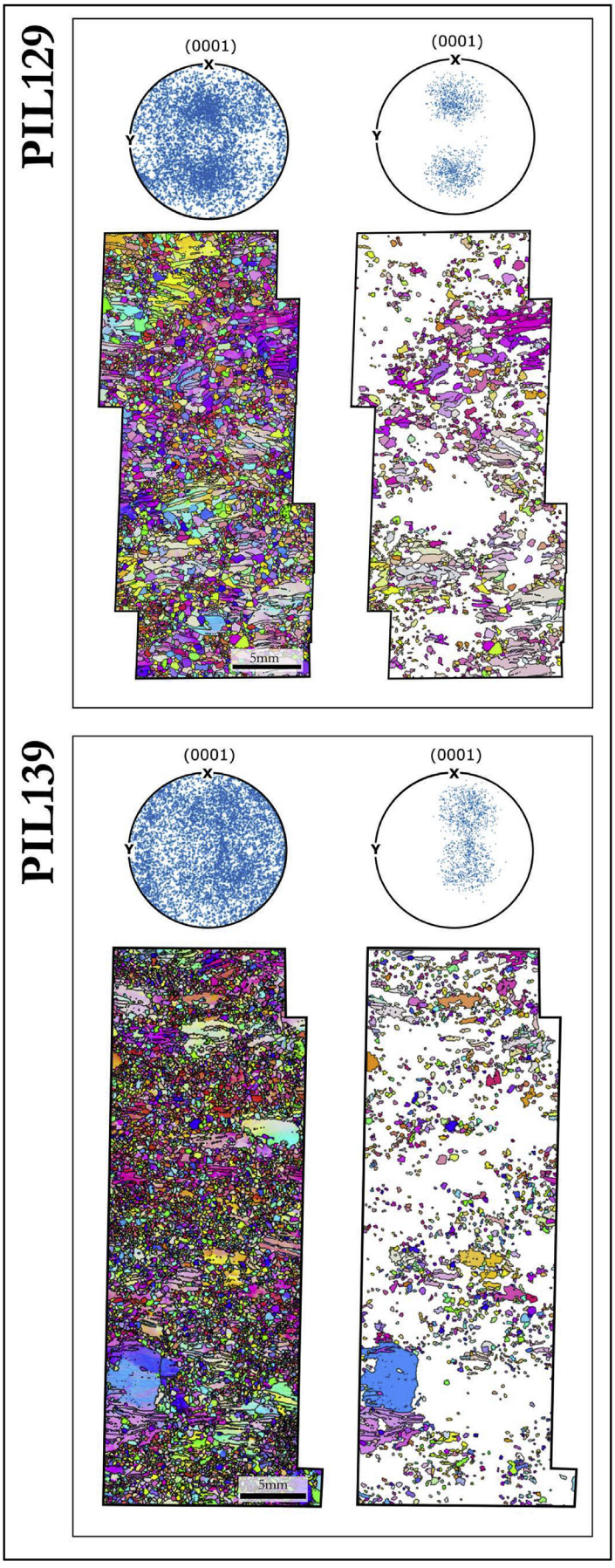

(caption on next page)

Fig. 7. Orientation maps of the group 2 samples along with lower hemisphere, equal area pole figures showing *c*-axis orientations of a random selection of 10,000 pixels. Full maps are shown on the left. The maps on the right show only grains corresponding to clusters on the stereonets. Maps are coloured according to the crystallographic direction which is parallel to the compression direction, vertical, according to the inverse pole figure legend in Fig. 3.

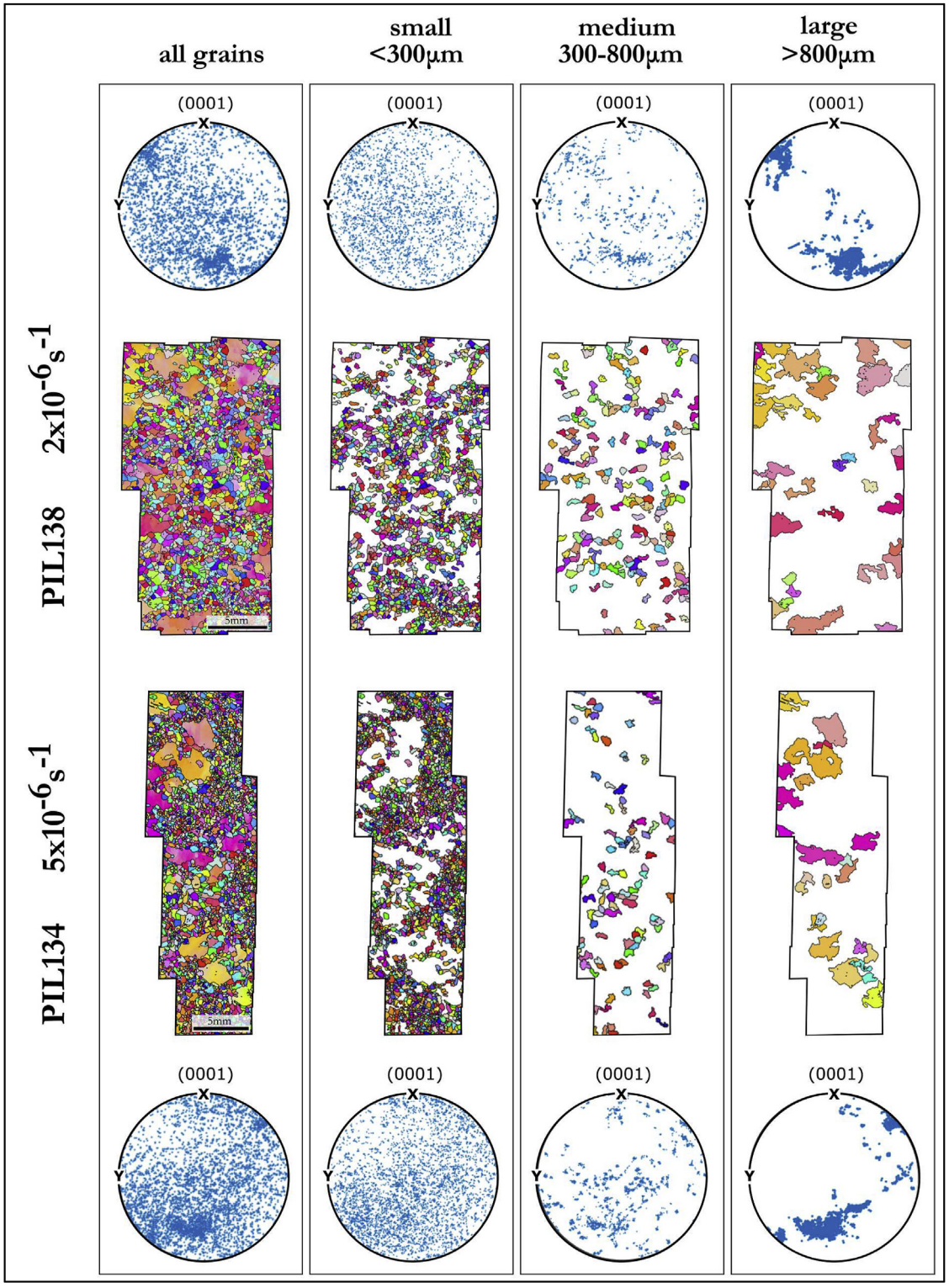

Fig. 8. Orientation maps of the group 3 samples, PIL138 and PIL134, coloured by crystallographic direction parallel to the compression direction (vertical) according to the inverse pole figure legend in Fig. 3, accompanied by lower hemisphere, equal area pole figures of a random selection of 10,000 pixels alongside contoured figures of all indexed pixels. Maps are segregated by grain size, from left to right: all grains; "small" grains < 300 μm in size; "medium" grains 300–800 μm in size; "large" grains > 800 μm in size. Scale is the same for all maps.

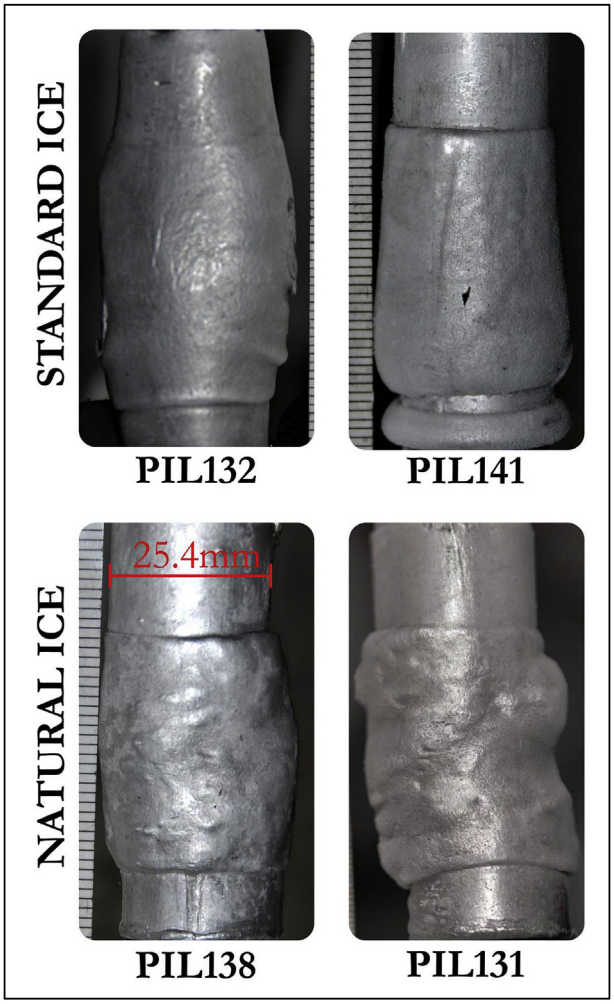

Fig. 9. Photographs of standard ice (upper) and natural ice (lower) samples after deformation, still encased in indium jackets. The diameter of the upper piston in all photographs is 25.4 mm.

(where applicable). These stress data are recorded in Table 2.

In the standard ice, at all strain rates, stress increases until reaching a sharp peak at strains of 0.02–0.04 and relaxes back to approach a constant flow stress. The natural ice samples behave less consistently. With the exception of PIL134 and PIL139, which broadly follow this standard ice pattern, all other natural samples have a yield stress much closer to the flow stress, and in some cases stress increases continuously beyond the yield point. All natural ice samples have a significantly lower yield stress than the standard ice samples at equivalent rates, with the exception of PIL134, which is similar to the standard ice values.

Fig. 11 shows the strain rate plotted against the yield stress for all experiments. The data are segregated by initial CPO (by symbol shape, solid fitted lines) and by final microstructural characteristics (see microstructural description: symbol fill colour, dashed fitted lines). The grain size exponent (n) is displayed on the graph for each grouping with a reasonable linear fit. The group of three experiments on samples with starting orientation of shortening 90° to the *c*-axis orientation plane of the original core are the only set of three (aside from standard ice) which approximate a linear trend, with its gradient indicating a stress exponent of $n = 2.5$. The standard ice samples give a linear trend indicating a stress exponent of $n = 4.1$.

4. Mechanisms of deformation

These experiments demonstrate that anisotropic natural ice can change its CPO entirely within strains of $\varepsilon = 0.2$. It is a dramatic change, with original grain orientations changing by up to 90°. Overall, the natural samples behaved significantly more weakly than pure synthetic samples under the same conditions. As pores were allowed to close prior to deformation and so porosity should not be a major factor, this is likely an effect of chemical impurities in the natural ice, which has been shown to cause weakening in both single crystal (Jones and Glen, 1969b) and polycrystalline ice (Hammonds, 2016). The effect of chemical impurities in these samples is a topic for further investigation.

The mechanisms through which deformation was accommodated and the CPO change took place were much more heterogeneously distributed in the natural ice than in synthetic, initially isotropic samples, as evidenced by the uneven sample surface morphology (Fig. 9). All of the re-deformed natural samples have large grains with lobate boundaries which define strongly the CPO, and smaller grains with straighter boundaries with a more diffuse CPO. The grain sizes of the finer-grained fraction after deformation are much smaller than in the original material and have a similar range to the final grain sizes in standard ice. The smaller grains are almost certainly newly recrystallised grains. The larger grains are larger than any grains developed in the standard ice experiments or grains developed from fine (0.2–1 mm) synthetic starting materials even at warmer temperatures (e.g. Montagnat et al., 2015; Qi et al., 2017; Vaughan et al., 2017), and are most likely remnants from the original material. There are recrystallised grains occurring at the intersections of straight subgrain boundaries in many samples, and within larger grains (e.g. Fig. 6) and subgrain boundaries forming at the margins of larger grains, often defining subgrains of a similar size to the adjacent recrystallised grains. Alongside the higher occurrence of low-angle boundaries than would be predicted from the CPO, these observations suggest that a process of recrystallisation by subgrain rotation is active (Wheeler et al., 2001; Bestmann and Prior, 2003; Qi et al., 2017). If the fine grains had been nucleated by bulging mechanisms associated with grain boundary migration, the recrystallised grains would be expected to have the same orientations as their parent grains (Doherty et al., 1997; Duval et al., 2012) and need not be the same size as subgrains (Halfpenny et al., 2006). The similar orientation of maxima of the CPOs of the small grains and large grains is consistent with subgrain rotation polygonisation, as intracrystalline grains (those nucleated within parent grains) formed by this process are likely to have orientations similar to their hosts, while intercrystalline grains (those nucleated at parent grain boundaries) formed would have more ambiguous orientations (Avé Lallemant, 1985; Llorens et al., 2017; Gomez-Rivas et al., 2017).

5. A model for microstructural evolution

A common element in all the natural samples is that the CPO of the original grains has changed substantially during the laboratory deformation. Further understanding of deformation mechanisms comes from understanding the processes by which this is achieved. A key observation is that all of the samples deformed in the 90° orientation had no original grains in the orientation of the maxima of the final CPO. Furthermore, there are very few large grains close to the orientation of original grains. If the interpretation of large grains as remnants of the original grains is correct, then these grains have undergone substantial rotation. The rotation process potentially comprises two elements. One is lattice rotation due to sliding on the basal plane. The second is grain rotation due to deformation of the surrounding matrix of finer grains. The CPO of the finer grains is a more diffuse equivalent of the large grain CPO, a characteristic which is consistent with a component of deformation by grain boundary sliding (GBS) (Bestmann and Prior, 2003; Jiang et al., 2000; Storey and Prior, 2005).

The grain size dependency of GBS (Goldsby and Kohlstedt, 1997,

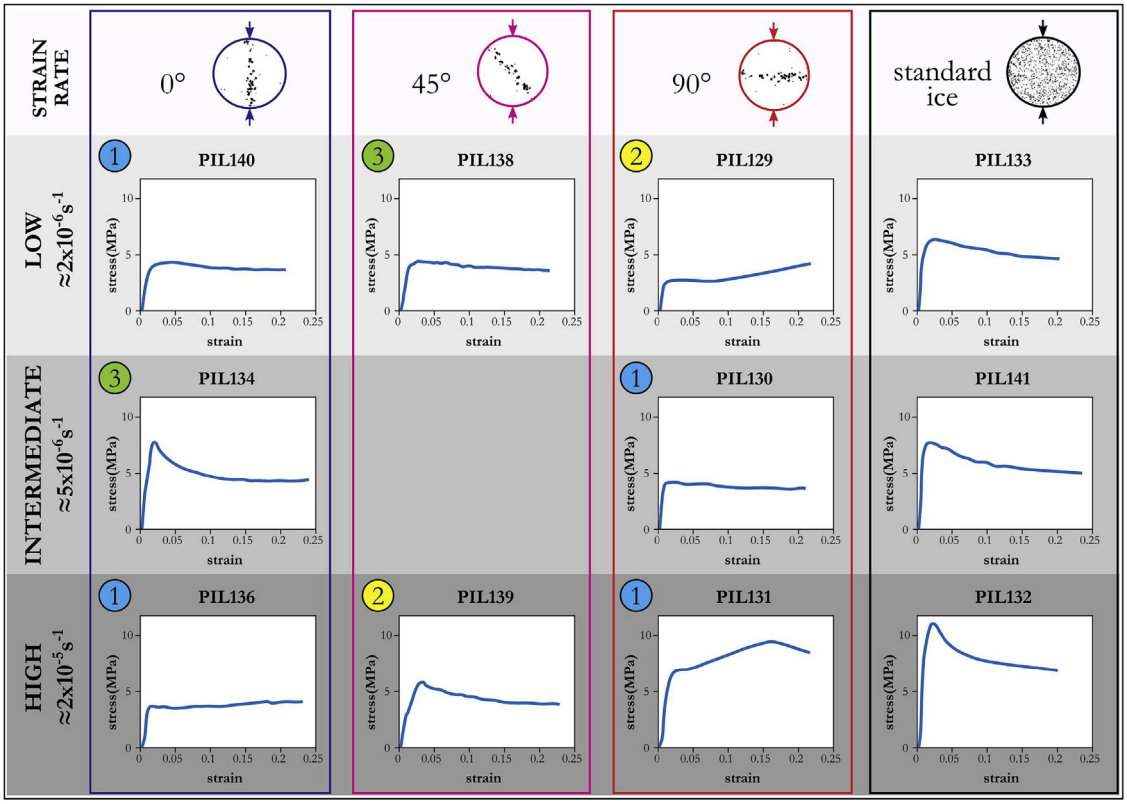

Fig. 10. Plots of axial stress *vs.* true strain (equation (1)) for all experiments. Each column shows all the experiments with a particular initial CPO, indicated by the stereonet at the top of the column. In each column data are organised by increasing strain rate downwards with the strain rates shown on the left-hand side. Circled numbers denote microstructural grouping, as discussed in the text. Column border colours and numbered circle fill colours are used to indicate initial CPO and microstructural group in Fig. 11. (For interpretation of the references to colour in this figure legend, the reader is referred to the Web version of this article.)

2001; Goldsby, 2006) would favour faster strain rates in finer grained parts of the sample compared to coarser grains under the same deformation conditions. The bulges on the sample surfaces (Fig. 9) have similar sizes to the spacing between connected fine-grained layers, and could reflect the strain rate heterogeneity in fine and coarse grains (Seidemann, 2018). A grain size dependence of −1.4 (Goldsby and Kohlstedt, 1997) gives a rate of GBS in ice with a 200 μm grain size to be 25 times faster than that of ice with a 2 mm grain size at the same stress and temperature. The strain rate attributed to GBS must be added to the strain rate attributed to dislocation creep (Goldsby and Kohlstedt, 2001). If we calculate the relative strain rates of fine to coarse ice using the Goldsby (2006) composite flow law (using a corrected A value of 1.2×10^4 MPa^{-4}s^{-1} for dislocation creep), ice with grain sizes of 100, 150 and 200 micrometres deforms at 2, 1.5 and 1.3 times the rate of ice with grain sizes on a millimetre scale (this calculation is relatively insensitive to the size of the coarse ice) at axial normal stresses of 5 MPa and a temperature of −30 °C. At present such a calculation has a high level of uncertainty, but it suggests that rigid rotation of grains controlled by GBS of the fine-grained ice can generate a significant component of remnant grain rotation. This is consistent with the fact that the large grains are not strongly shaped; axial ratios of ~1.4 (related to the axial strain of 0.2) would be expected if rotation were controlled entirely by slip on the basal plane. Given that the coarse grains develop strong CPOs, other mechanisms must also contribute to remnant grain rotation. We suggest that the basal plane orientation controls the sense of remnant grain rotation, so that the grain rotation contributes to the CPO development.

The process outlined above has many parallels to naturally-occurring rock shear zones, where a common interpretation is that larger clasts rotate rigidly when they are surrounded by a matrix with a much smaller grain size, which can simply be a recrystallised fraction of the clast material (Passchier and Simpson, 1986). The mechanism for rotation is slip at the interface between a large, rigid object and localised deformation of the weaker, recrystallised material (Ildefonse and Mancktelow, 1993; Bestmann et al., 2006).

5.1. Heterogeneity in sample behaviour

Microstructures suggest a similar set of active mechanisms in all the samples. It is quite reasonable to expect the same balance of mechanisms in material with the same grain size and deformation conditions (e.g. natural ice samples deformed at the same strain rate and temperature). If the active deformation mechanisms are the same in all samples, why do they give rise to different microstructures and CPOs (groups 1, 2 and 3 as described in section 3.2) in a way which does not appear to be related to their starting orientation relative to the CPO?

Fig. 12 provides an overview of the microstructural evolution of the natural samples. While in all cases subgrain rotation recrystallisation led to the formation of an interconnected network of fine grains facilitating rotation of larger remnant grains, the final microstructure of the samples varied. We suggest that the three types of final microstructure have come about as a result of biases in the orientations of the original grains, within the constraints of the known girdle CPO. It is likely that the large size of the original grains relative to the sample diameter means that any given cross section of the sub-cores may contain only a few grains (the sub-core cross section in Fig. 1 contains < 30 grains). These few grains then have a large effect on the behaviour of an entire sample. This effect must be large enough to have a greater control on behaviour than the orientation of the sample to the CPO.

The group 1 sample microstructure (Fig. 12, upper right) is likely related to a bias in original grain orientations toward both 0° and 90° from the compression direction. Grains at or close to those orientations

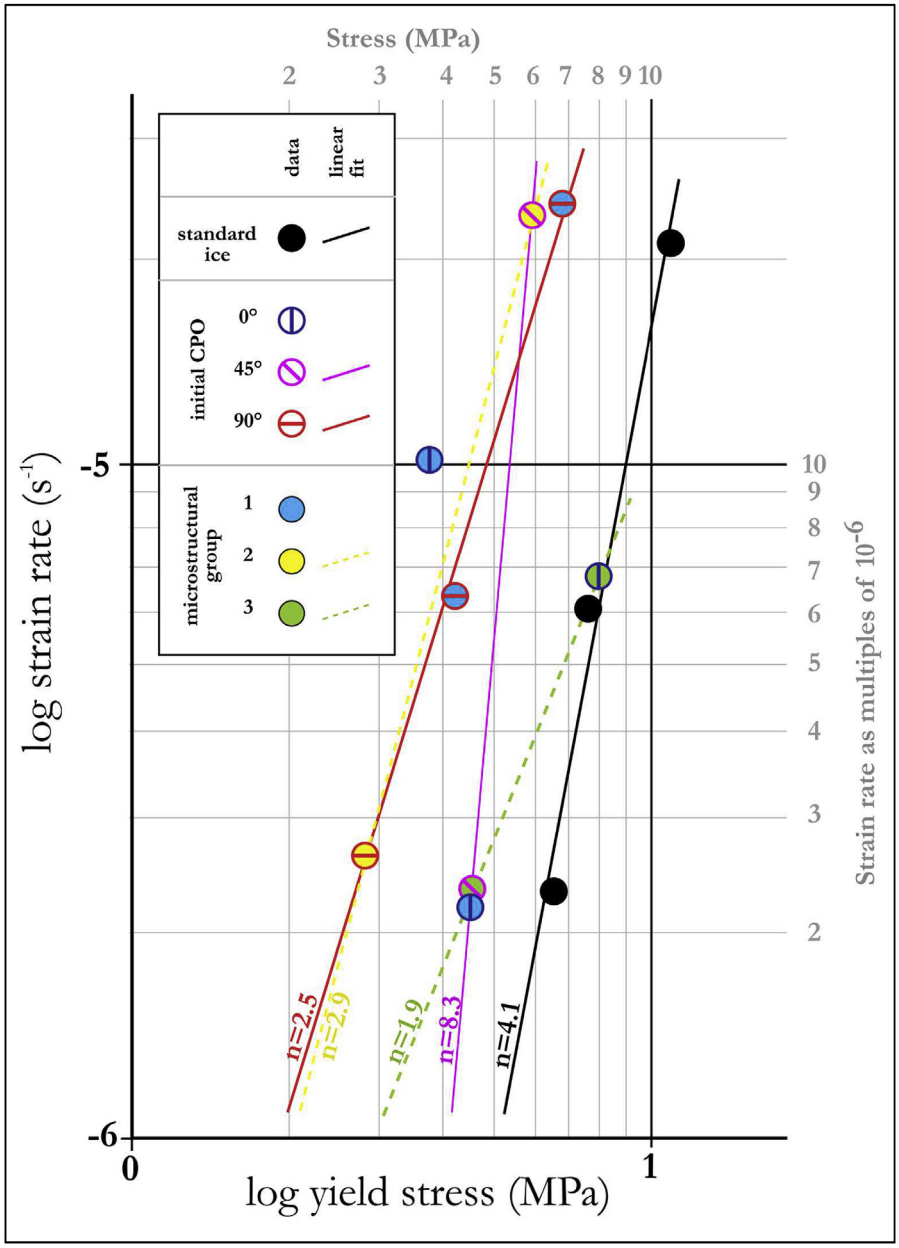

Fig. 11. Plots of log yield stress versus log strain rate for all experiments, segregated by initial orientation of CPO relative to compression (symbols show the CPO schematically and have border colours corresponding to initial CPO. Linear fit is shown by solid lines with colour indicative of initial CPO), and final microstructural characteristics (symbol fill colour corresponds to microstructural group. Linear fit is shown by dashed lines with colour indicative of microstructural group). (For interpretation of the references to colour in this figure legend, the reader is referred to the Web version of this article.)

must have a low Schmid factor and therefore preferentially recrystallise, allowing the fine-grained matrix to form very early in the deformation process so that remnant grains could easily rotate to form a strong cluster CPO.

The group 2 sample microstructure (Fig. 12, middle right) is likely related to a bias in original grain orientations at 90° to the compression direction alone. As these grains are oriented with basal planes parallel to compression, they are likely to undergo kinking early in the deformation process (Wilson et al., 1986), thus "locking" into place instead of rotating or fully recrystallising and preventing the formation of a fine grain network as extensive as in the group 1 samples. Kinked segments in these samples define a double-cluster CPO. Grains close to this orientation may be able to rotate with the aid of the recrystallised matrix until kinking occurs, through basal slip and grain boundary sliding as in the group 1 samples, and it is possible that continued deformation of these samples would lead to melange-style flow once a large enough proportion of grains had fully recrystallised.

The group 3 sample microstructure (Fig. 12, bottom right) is likely related in part to a more even distribution in grain orientations within the known CPO, and in part to an element of shear during the deformation process. The more normal distribution of grain sizes suggests that grain nucleation and growth was more evenly spread instead of being localised in some grains. The inclined CPO is most easily explained by the presence of shear, in cases where upper and lower pistons may have become slightly offset during the experiment.

5.2. Applications to ice flow modelling

As the microstructural behaviour of the ice appears to be largely controlled by a bias in orientations that would not be present in larger

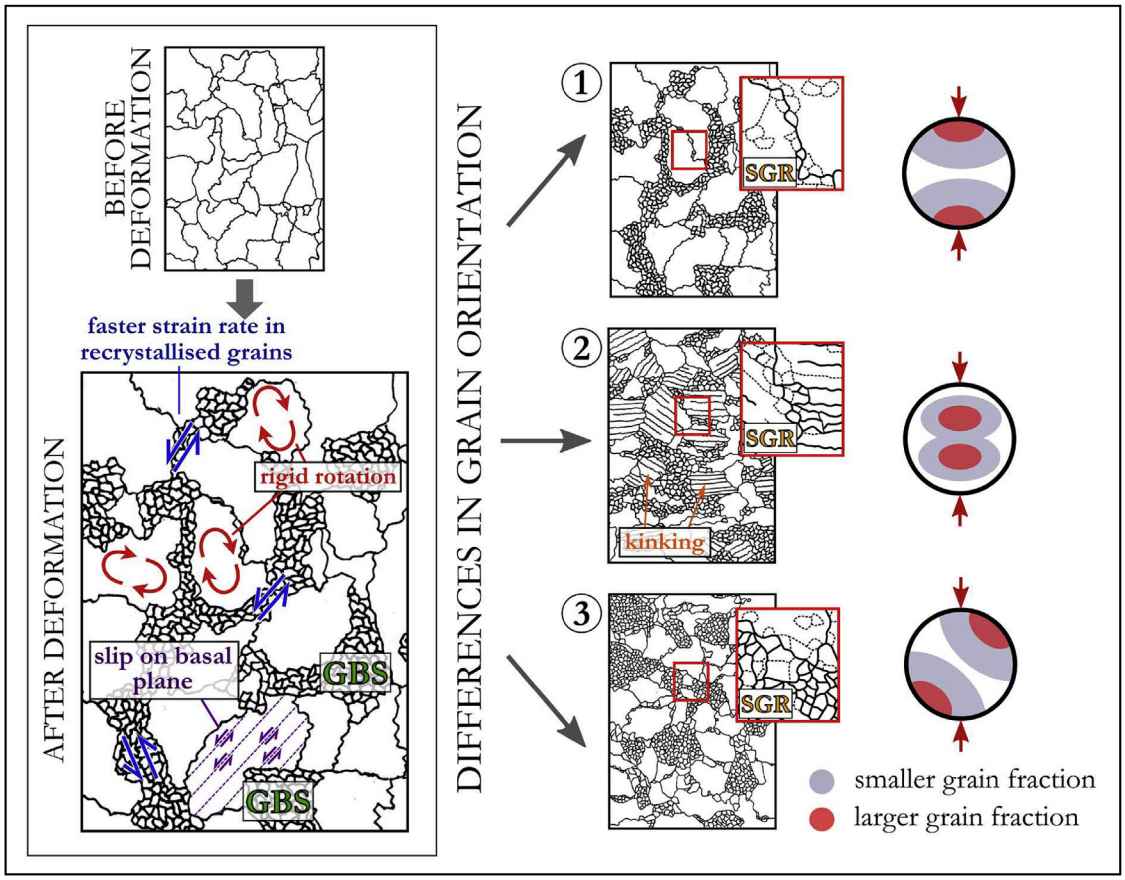

Fig. 12. Schematic representation of the evolution of the microstructures developed during deformation of the natural samples. The left-hand side shows an interpretation of processes common to all samples. The right-hand side illustrates how bias in the original grain population may lead to the different final CPOs and microstructural characteristics (groups 1 to 3) observed. GBS = grain boundary sliding. SGR = subgrain rotation.

ice masses, care should be taken when interpreting these results. The mechanical behaviour of the natural ice samples diverged significantly beyond the yield stress, and so further study would be required for any observations of longer-term flow behaviour to be robust. However, we suggest three key observations from this study which are robust, and are worthy of specific attention in future ice flow models.

Firstly, we have shown that natural ice yields at a significantly lower stress than pure standard ice deformed under the same conditions (see section 3.1; Fig. 4). We suggest that this is due to the presence of soluble impurities in the ice, which have been observed to cause rheological weakening in single crystals (Jones and Glen, 1969b; Baker et al., 2003). This would suggest that instead of using flow laws with stress exponents of $n \approx 3$ based on experiments in pure ice (Glen, 1955; Budd and Jacka, 1989; Wilson et al., 2014), a higher value corresponding to a lower viscosity would be more appropriate. Durham et al. (1983), Treverrow et al. (2012) and Qi et al. (2017) have suggested values closer to $n \approx 4$.

Secondly, we have shown that the CPO of deforming ice can change completely within strains of 0.2. If this is also the case in larger ice masses, strain rates may change significantly within the period directly following a change in stress conditions. This rapid change in strain rates should be represented in models.

Thirdly, on a micro scale, a clear geometric segregation developed in these samples between larger and finer grains, and strain appears to be accommodated heterogeneously, focussed within the finer-grained sections. When modelling the grain-scale behaviour of deforming ice, it is necessary to consider the presence of heterogeneities in grain size and strain accommodation.

To make more robust inferences, similar experiments with much larger samples or finer grain sizes would be necessary. However, these experiments do reveal important differences between natural and synthetic ice which may inform the assumptions built into ice flow models.

6. Summary and conclusions

1. We drilled sub-cores from a sample of natural glacial ice with coarse grain size and a strong CPO defined by *c*-axes lying in a vertical plane. Sub cores had core axes parallel, 45° and perpendicular to the pole to the plane of *c*-axes. We deformed these sub-cores under 30 MPa confining pressure (to prevent brittle behaviour), at three different strain rates, at −30 °C, to final strains of 0.2. Reference samples of standard ice, an isotropic synthetic polycrystalline ice with ~230 μm grain size, were deformed under the same conditions. Microstructures and crystallographic preferred orientations (CPOs) of all samples were extracted from cryo-EBSD data.
2. The natural ice deformed here behaves more weakly than standard ice at similar strain rates under the same experimental conditions. This is most likely a mechanical softening effect caused by chemical impurities in the natural ice.
3. Mechanical behaviour and microstructural characteristics of deformed natural ice do not correspond to the orientation of compression to the original CPO. Yield stresses increase with increasing strain rate, only in samples where all grains had *c*-axes perpendicular to compression (giving a stress exponent of $n = 2.5$). In other samples, where *c*-axes have a wider range of angles to compression the yield stress does not vary in a consistent way with strain rate. Beyond the yield stress, the flow stress evolution shows no pattern related to original CPO or deformation conditions. It is unlikely that any of the natural samples had achieved true steady-state flow when the experiments were stopped at strains of 0.2. The mechanical and

microstructural inconsistencies relate to the large initial grain size relative to sample size. This allowed small biases in orientation within the confines of this known CPO to have a disproportionately large effect on behaviour. It is likely that had the experiments continued to higher strains, the microstructure and mechanics would have continued to evolve.

4. Natural samples, after deformation, comprise a mix of coarse (~1–2 mm) remnant grains and fine (~100–200 μm) recrystallised grains. The fine grains form a connected network in all samples. Coarse grains do not have a strong or consistent shape preferred orientation.
5. All natural samples develop an entirely new CPO within strains of 0.2. In all cases the large grains define a very strong CPO comprising either one or two maxima. The recrystallised grains have a CPO with the same shape and symmetry (maxima in the same orientation), but these CPOs are more weakly developed. The CPO in the "standard" ice is a cluster of *c*-axes parallel to compression; the strength of this CPO is similar to the strength of the CPO of the recrystallised grains in the natural samples. A cluster parallel to compression is also the most common CPO in the re-deformed natural samples (4 samples). The other natural samples have CPOs with a single *c*-axis cluster slightly oblique (~20°) to compression (2 samples) or two *c*-axis clusters at ~45° to compression (2 samples) and contained within a plane that includes the compression axis.
6. Lattice distortion and subgrains indicate that dislocation creep and recovery were important during deformation. Subgrains with similar sizes to the recrystallised grains suggest that recrystallisation included a process of subgrain rotation recrystallisation. We suggest a model where deformation in the connected network of recrystallised grains occurs with a significant component of grain boundary sliding. This enables large grains to rotate by a combination of glide on the basal plane and rigid rotation to define a very strong CPO. We suggest that CPO in the recrystallised grains is weakened by the GBS and by analogy GBS is an important process in the "standard" ice samples.
7. After recrystallisation and grain rotation had commenced, three slightly different final microstructures could develop, characterised respectively by either a strong vertical cluster, double-cluster, or inclined cluster CPO. We suggest that these differences are related to biases in grain orientation within the known girdle CPO, as the original grain size is very large in comparison with the sample size.

Acknowledgements

We are grateful to Marianne Negrini and Sheng Fan for help with the EBSD analysis, Travis Hager for assistance in the laboratory, Pat Langhorne for the use of her cold rooms, and Yeongcheol Han for ice sampling. This research was made possible by funding provided by the Todd Foundation, the New Zealand Antarctic Research Institute, the Trans-Antarctic Association, KOPRI project PM18030 (20140409), Marsden Fund UOO052 of the Royal Society of New Zealand, and a University of Otago Research Grant 2018.

We gratefully acknowledge Maria-Gema Llorens and Christopher Gerbi for their very constructive comments on this manuscript.

References

Alley, R.B., 1992. Flow-law hypotheses for ice-sheet modeling. J. Glaciol. 38, 245–256.
Avé Lallemant, H.G., 1985. Subgrain rotation and dynamic recrystallisation of olivine, upper mantle diapirism, and extension of the Basin-and-Range province. Tectonophysics 119, 89–117.
Bachmann, F., Hielscher, R., Schaeben, H., 2011. Grain detection from 2d and 3d EBSD data — specification of the MTEX algorithm. Ultramicroscopy 111, 1720–1733. https://doi.org/10.1016/j.ultramic.2011.08.002.
Baker, I., Cullen, D., Iliescu, D., 2003. The microstructural location of impurities in ice. Can. J. Phys. 81, 1–9. https://doi.org/10.1139/p03-030.
Baker, R.W., Gerberich, W.W., 1979. The effect of crystal size and dispersed-solid inclusions on the activation energy for creep. J. Glaciol. 24, 179–194.
Barnes, P.R.F., Mulvaney, R., Robinson, K., Wolff, E.W., 2002. Observations of polar ice from the Holocene and the glacial period using the scanning electron microscope. Ann. Glaciol. 35, 559–566. https://doi.org/10.3189/172756402781816735.
Barnes, P.R.F., Wolff, E.W., 2004. Distribution of soluble impurities in cold glacial ice. J. Glaciol. 50, 311–324. https://doi.org/10.3189/172756504781829918.
Bestmann, M., Prior, D.J., 2003. Intragranular dynamic recrystallization in naturally deformed calcite marble: diffusion accommodated grain boundary sliding as a result of subgrain rotation recrystallization. J. Struct. Geol. 25, 1597–1613. https://doi.org/10.1016/S0191-8141(03)00006-3.
Bestmann, M., Prior, D.J., Grasemann, B., 2006. Characterisation of deformation and flow mechanics around porphyroclasts in a calcite marble ultramylonite by means of EBSD analysis. Tectonophysics 413, 185–200. https://doi.org/10.1016/j.tecto.2005.10.044.
Budd, W.F., Warner, R.C., Jacka, T.H., Li, J., Treverrow, A., 2013. Ice flow relations for stress and strain-rate components from combined shear and compression laboratory experiments. J. Glaciol. 59, 374–392. https://doi.org/10.3189/2013JoG12J106.
Budd, W.F., Jacka, T.H., 1989. A review of ice rheology for ice sheet modelling. Cold Reg. Sci. Technol. 16, 107–144.
Castelnau, O., Shoji, H., Mangeney, A., Milsch, H., Duval, P., 1998. Anisotropic behavior of GRIP ices and flow in Central Greenland. Earth Planet. Sci. Lett. 154, 307–322.
Dahl-Jensen, D., Thorsteinsson, T., Alley, R., Shoji, H., 1997. Flow properties of the ice from the Greenland Ice Core Project ice core: the reason for folds? J. Geophys. Res. 102, 26831–26840.
Dierckx, M., Peternell, M., Schroeder, C., Tison, J., 2014. Influence of pre-existing microstructure on mechanical properties of marine ice during compression experiments. J. Glaciol. 60, 576–586. https://doi.org/10.3189/2014JoG13J154.
Doherty, R.D., Hughes, D.A., Humphreys, F.J., Jonas, J.J., Juul Jensen, D., Kassner, M.E., King, W.E., McNelley, T.R., McQueen, H.J., Rollett, A.D., 1997. Current issues in recrystallization: a review. Mater. Sci. Eng. A238, 219–274. https://doi.org/10.1016/S0921-5093(97)00424-3.
Durham, W.B., Heard, H.C., Kirby, S.H., 1983. Experimental deformation of polycrystalline H_2O ice at high pressure and low temperature: preliminary results. J. Geophys. Res. 88, 377–392. https://doi.org/Doi 10.1029/Jb088is01p0b377.
Duval, P., Ashby, M.F., Andermant, I., 1983. Rate-controlling processes in the creep of polycrystalline ice. J. Phys. Chem. 87, 4066–4074. https://doi.org/10.1021/j100244a014.
Duval, P., Louchet, F., Weiss, J., Montagnat, M., 2012. On the role of long-range internal stresses on grain nucleation during dynamic discontinuous recrystallization. Mater. Sci. Eng. A 546, 207–211. https://doi.org/10.1016/j.msea.2012.03.052.
Gao, X., Jacka, T., 1987. The approach to similar tertiary creep rates for Antarctic core ice and laboratory prepared ice. J. Phys. Colloq. 48, 289–296.
Glen, J.W., 1955. The creep of polycrystalline ice. Proc. Roy. Soc. A Math. Phys. Eng. Sci. 228, 519–538. https://doi.org/10.1098/rspa.1955.0066.
Goldsby, D.L., 2006. Superplastic flow of ice relevant to glacier and ice-sheet mechanics. In: Knight, P. (Ed.), Glacier Science and Environmental Change. Wiley-Blackwell, Chichester, pp. 308–314.
Goldsby, D.L., Kohlstedt, D.L., 1997. Grain boundary sliding in fine-grained ice I. Scr. Mater. 37, 1399–1406. https://doi.org/10.1016/S1359-6462(97)00246-7.
Goldsby, D.L., Kohlstedt, D.L., 2001. Superplastic deformation of ice: experimental observations. J. Geophys. Res. 106, 11017–11030.
Gomez-Rivas, E., Griera, A., Llorens, M.G., Bons, P.D., Lebensohn, R.A., Piazolo, S., 2017. Subgrain rotation recrystallization during shearing: insights from full-field numerical simulations of halite polycrystals. J. Geophys. Res.: Solid Earth 122, 8810–8827. https://doi.org/10.1002/2017JB014508.
Halfpenny, A., Prior, D.J., Wheeler, J., 2006. Analysis of dynamic recrystallization and nucleation in a quartzite mylonite. Tectonophysics 427, 3–14. https://doi.org/10.1016/j.tecto.2006.05.016.
Hambrey, M.J., 1975. The origin of foliation in glaciers: evidence from some Norwegian examples. J. Glaciol. 14, 181–185.
Hammonds, K., 2016. The Effects of Soluble Impurities on the Mechanical Behaviour of Polycrystalline Ice and Laboratory Investigations on the Thermophysical Properties of Ice-snow Interfaces (Thesis, Doctor of Philosophy). Dartmouth College.
Hammonds, K., Baker, I., 2016. The effects of Ca++ on the strength of polycrystalline ice. J. Glaciol. 1–9. https://doi.org/10.1017/jog.2016.84.
Hudleston, P.J., 2015. Structures and fabrics in glacial ice: a review. J. Struct. Geol. 81, 1–27. https://doi.org/10.1016/j.jsg.2015.09.003.
Hudleston, P.J., Hooke, R.L., 1980. Cumulative deformation in the Barnes Ice Cap and implications for the development of foliation. Tectonophysics 66, 127–146. https://doi.org/10.1016/0040-1951(80)90042-6.
Hughes, T., 2009. Modeling ice sheets from the bottom up. Quat. Sci. Rev. 28, 1831–1849. https://doi.org/10.1016/j.quascirev.2009.06.004.
Ildefonse, B., Mancktelow, N.S., 1993. Deformation around rigid particles: the influence of slip at the particle/matrix interface. Tectonophysics 221, 345–359. https://doi.org/10.1016/0040-1951(93)90166-H.
Jiang, Z., Prior, D.J., Wheeler, J., 2000. Albite crystallographic preferred orientation and grain misorientation distribution in a low-grade mylonite: implications for granular flow. J. Struct. Geol. 22, 1663–1674. https://doi.org/10.1016/S0191-8141(00)00079-1.
Jones, S.J., Glen, J.W., 1969a. Mechanical properties of single crystals of pure ice. J. Glaciol. 8, 463–473.
Jones, S.J., Glen, J.W., 1969b. The effects of dissolved impurities on the mechanical properties of ice crystals. Phil. Mag. 19, 13–24.
Kamb, B., 1972. In: Experimental Recrystallization of Ice under Stress. Flow and Fracture of Rocks, vol. 16. American Geophysical Union Geophysical Monograph, pp. 211–241 California I. of T.
Llorens, M.G., Griera, A., Steinbach, F., Bons, P.D., Gomez-Rivas, E., Jansen, D.,

Roessiger, J., Lebensohn, R.A., Weikusat, I., 2017. Dynamic recrystallization during deformation of polycrystalline ice: insights from numerical simulations. Phil. Trans. Roy. Soc. A Math. Phys. Eng. Sci. 375. https://doi.org/10.1098/rsta.2015.0346.

Mainprice, D., Bachmann, F., Hielscher, R., Schaeben, H., 2015. Descriptive tools for the analysis of texture projects with large datasets using MTEX: strength , symmetry and components. Geol. Soc. Lond. Spec. Publ. 409, 251–271.

Means, W., 1976. Stress and Strain. Basic Concepts of Continuum Mechanics for Geologists. Springer-Verlag, New York, Berlin.

Montagnat, M., Chauve, T., Barou, F., Tommasi, A., Beausir, B., Fressengeas, C., 2015. Analysis of dynamic recrystallization of ice from EBSD orientation mapping. Front. Earth Sci. 3, 1–13. https://doi.org/10.3389/feart.2015.00081.

Passchier, C.W., Simpson, C., 1986. Porphyroclast systems as kinematic indicators. J. Struct. Geol. 8, 831–843.

Pauling, L., 1935. The structure and entropy of ice and of other crystals with some randomness of atomic arrangement. J. Am. Chem. Soc. 57, 2680–2684. https://doi.org/10.1021/ja01315a102.

Pearce, M.A., 2015. EBSDinterp 1.0 : a MATLAB ® program to perform microstructurally constrained interpolation of EBSD data. Microsc. Microanal. 21, 985–993. https://doi.org/10.4225/08/5510090C6E620.

Prior, D.J., Oyle, A.P., Brenker, F., Cheadle, M.C., Day, A., Lopez, G., Peruzzo, L., Potts, G.J., Reddy, S.R., Spiess, R., Timms, N.E., Trimby, P., Wheeler, J., Zetterström, L., 1999. The application of electron backscatter diffraction and orientation contrast imaging in the SEM to textural problems in rocks. Am. Mineral. 84, 1741–1759.

Prior, D.J., Lilly, K., Seidemann, M., Vaughan, M., Becroft, L., Easingwood, R., Diebold, S., Obbard, R., Daghlian, C., Baker, I., Caswell, T., Golding, N., Goldsby, D., Durham, W.B., Piazolo, S., Wilson, C.J.L., 2015. Making EBSD on water ice routine. J. Microsc. 259 n/a-n/a. https://doi.org/10.1111/jmi.12258.

Qi, C., Goldsby, D.L., Prior, D.J., 2017. The down-stress transition from cluster to cone fabrics in experimentally deformed ice. Earth Planet. Sci. Lett. 471, 136–147. https://doi.org/10.1016/j.epsl.2017.05.008.

Rignot, E., Casassa, G., Gogineni, P., Krabill, W., Rivera, A., Thomas, R., 2004. Accelerated ice discharge from the Antarctic Peninsula following the collapse of Larsen B ice shelf. Geophys. Res. Lett. 31, 0–4. https://doi.org/10.1029/2004GL020697.

Seidemann, M., 2018. Microstructural Evolution of Polycrystalline Ice during Confined Creep Testing. Ph.D. thesis. University of Otago.

Shoji, H., Langway, C.C., 1982. Air hydrate inclusions in fresh ice core. Nature. https://doi.org/10.1038/298548a0.

Stern, L., Durham, W.B., Kirby, S.H., 1989. Grain-size-induced weakening of H_2O ices i and ii and associated anisotropic recrystallisation. J. Geophys. Res. 29, 267–274.

Storey, C.D., Prior, D.J., 2005. Plastic deformation and recrystallization of garnet: a mechanism to facilitate diffusion creep. J. Petrol. 46, 2593–2613. https://doi.org/10.1093/petrology/egi067.

Treverrow, A., Budd, W.F., Jacka, T.H., Warner, R.C., 2012. The tertiary creep of polycrystalline ice: experimental evidence for stress-dependent levels of strain-rate enhancement. J. Glaciol. 58, 301–314. https://doi.org/10.3189/2012JoG11J149.

Treverrow, A., Warner, R.C., Budd, W.F., Craven, M., 2010. Meteoric and marine ice crystal orientation fabrics from the Amery Ice Shelf , East Antarctica. J. Glaciol. 56, 877–890.

Vaughan, M.J., Prior, D.J., Jefferd, M., Brantut, N., Mitchell, T.M., Seidemann, M., 2017. Insights into anisotropy development and weakening of ice from in situ P wave velocity monitoring during laboratory creep. J. Geophys. Res.: Solid Earth 122, 7076–7089. https://doi.org/10.1002/2017JB013964.

Wang, Y., Thorsteinsson, T., Kipfstuhl, J., Miller, H., Dahl-Jensen, D., Shoji, H., 2002. A vertical girdle fabric in the NorthGRIP deep ice core, North Greenland. Ann. Glaciol. 35, 515–520. https://doi.org/10.3189/172756402781817301.

Warner, R.C., Budd, W.F., 1998. Modelling the long-term response of the Antarctic ice sheet to global warming. Ann. Glaciol. 27, 161–168.

Wheeler, J., Prior, D.J., Jiang, Z., Spiess, R., Trimby, P.W., 2001. The petrological significance of misorientations between grains. Contrib. Mineral. Petrol. 141, 109–124. https://doi.org/10.1007/s004100000225.

Wilson, C.J.L., Burg, J.P., Mitchell, J.C., 1986. The origin of kinks in polycrystalline ice. Tectonophysics 127, 27–48.

Wilson, C.J.L., Peternell, M., Piazolo, S., Luzin, V., 2014. Microstructure and fabric development in ice: lessons learned from in situ experiments and implications for understanding rock evolution. J. Struct. Geol. 61, 50–77. https://doi.org/10.1016/j.jsg.2013.05.006.